Sustainable Energy & Fuels

Interdisciplinary research for the development of sustainable energy technologies

Accepted Manuscript

This article can be cited before page numbers have been issued, to do this please use: R. Valenza, S. Gadolini, I. Holmes-Gentle, F. Spanu, E. C. Corbos and S. Haussener, *Sustainable Energy Fuels*, 2026, DOI: 10.1039/D6SE00417B.

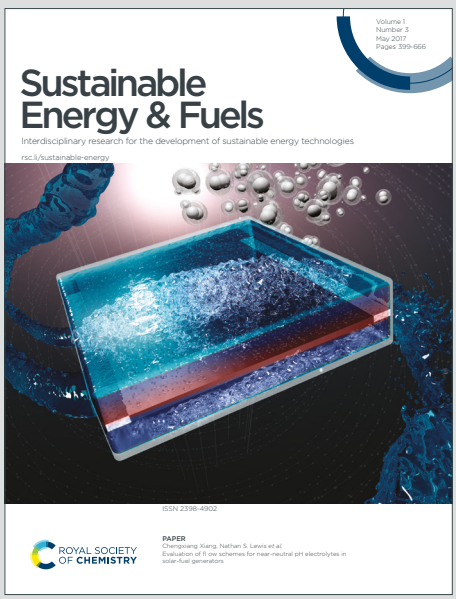

ROYAL SOCIETY OF CHEMISTRY

rsc.li/sustainable-energy

View Article Online
DOI: 10.1039/D6SE00417B

Journal Name

ARTICLE TYPE

Cite this: DOI: 00.0000/xxxxxxxxxx

Performance and stability of membrane-photoelectrode assemblies with $BiVO_4$ photoanodes for water splitting†

Roberto Valenza,[a] Sebastiano Gadolini,[b] Isaac Holmes-Gentle,[a] Francesco Spanu,[b] Elena C. Corbos[b] and Sophia Haussener[a,*]

Received Date
Accepted Date

DOI: 00.0000/xxxxxxxxxx

Membrane-photoelectrode assemblies are a promising device configuration to directly electrolyse liquid water or water vapour into hydrogen and oxygen using solar energy. For the first time, we studied the performance and the stability of membrane-photoelectrode assemblies with $BiVO_4$ photoanodes and CoPi co-catalysts on metallic felts at different temperatures. Upon illumination with simulated solar light, photocurrent densities of 0.23 mA cm^{-2} at 1 V *vs.* RHE were obtained with the proton-exchange ionomer and 0.06 mA cm^{-2} with anion-exchange ionomer, all using liquid water at 30 °C. Operation with liquid water at 56 °C reduced the onset potential difference in light and dark due to more severe recombination of charges, independent on the choice of ionomer. The (photoelectro)chemical corrosion reactions resulted in the dissolution of Bi, V, Mo and Co, which was accelerated by temperature. The dissolved species formed solid particles mainly containing vanadium in the proton-exchange membranes. Operation of proton-exchange membrane-photoelectrode assemblies with water vapour resulted in 85% decrease of the photocurrent density produced at 1 V *vs.* RHE as the hydration of the ionomer was reduced. The more acidic local pH at the ionomer-photoelectrode interface (compared to liquid water operation) accelerated the dissolution of the photoactive material in time, resulting in a faster decrease of the saturation current density. Membrane-photoelectrode assemblies have demonstrated to expand practical device configurations beyond conventional planar setups. The remaining performance gap with respect to planar photoelectrodes highlights the gains that systematic optimisation of membrane-photoelectrode assemblies can still unlock.

1 Introduction

Various device configurations have been proposed for the solar-driven conversion of water into hydrogen and oxygen using a photoelectrochemical (PEC) approach, i.e. with at least a semiconductor in direct contact with an electrolyte.[1] A membrane-photoelectrode assembly (MPEA) is a system in which a solid ionomer is used to ionically connect a semiconductor on a conductive substrate to another electrode.

The use of solid ionomer electrolytes allows operating the electrolyzer with pure water reactant feeds, either in liquid or gas phase. Humidity in the air can also be used, making the application attractive for locations with limited access to liquid water. Using humid air, the parasitic optical losses caused by bubble generation in liquid solutions may be avoided at the expense of earlier mass transport limitations.[2] Whilst hydrated solid ionomers typically have a lower ionic conductivity than concentrated liquid electrolytes,[3] their low hydrogen and oxygen permeability (in the order of 10^{-11} mol s^{-1} cm^{-2} bar^{-1})[4] allows for the use of thin membranes (*e.g.*, $\sim$100 μm thick) and high-purity hydrogen generation. This approach minimizes gaseous product crossover, reduces ohmic losses, and enhances partial load operation efficiency compared to systems using liquid electrolytes and porous separators.[5] The main disadvantage of solid ionomers is however their elevated price which currently limits their attractiveness for large-scale utilization.[6] Similar as for liquid electrolytes, some of the commercial ionomers also parasitically absorb light, potentially reducing the fraction of the solar spectrum reaching the photoelectrodes.

Monopolar solid ionomers operating at low temperature (below 80 °C) are divided in two categories depending on the type

* Corresponding author, E-mail: sophia.haussener@epfl.ch
[a] Laboratory of Renewable Energy Science and Engineering, Institute of Mechanical Engineering, École Polytechnique Fédérale de Lausanne, 1015 Lausanne, Switzerland.
[b] Johnson Matthey Technology Centre, Blounts Court Road, Reading RG4 9NH, United Kingdom.
† Electronic Supplementary Information (ESI) available: [details of any supplementary information available should be included here]. See DOI: 00.0000/00000000.

View Article Online
DOI: 10.1039/D6SE00417B

of ion which they can selectively transfer: cation-exchange (commonly called proton-exchange) or anion-exchange ionomers.[7,8] When properly hydrated, proton-exchange ionomers impose an acidic local environment at the interface with the photoelectrode (pH ≈ 2).[9] The low pH limits the choice of suitable semiconductors and co-catalysts which do not suffer from (photo)corrosion, especially for the photoanode performing the oxygen evolution reaction (OER).[10] Most of the commercial proton-exchange ionomers, i.e. Nafion™ of Chemours, are composed of perfluorinated alkylated substances (PFAS), whose production has been recently restricted due to their severe impact on environment and health.[11]

Anion-exchange ionomers are less developed apparent from shorter lifetimes than proton-exchange ionomers.[12] Good electrical insulating properties are achieved while introducing positively charged functional groups to ensure the transfer of hydroxyl anions when hydrated. Various backbones not necessarily relying on PFAS (*e.g.*, heteroatom-based polyaromatics, poly(arylene)s and polyolefins) can be used.[13] The local alkaline pH in the nanochannels of anion-exchange ionomers may be beneficial for the stability of a larger number of more common and less expensive materials like hematite (α-Fe_2O_3) photoanodes with co-catalysts based on transition metals like Co or Ni.[14,15]

Different metal oxide semiconductors have been tested in MPEA configuration. Metallic meshes of Ti or W were partially oxidized to create a thin layer of semiconductor (TiO_2 or WO_3, respectively) on their surface and then integrated in proton-exchange MPEAs.[16–18] Bismuth vanadate ($BiVO_4$) was deposited on Ti felts through dip-coating techniques and covered with proton-exchange ionomer to form MPEAs.[19,20] A record photocurrent density of 2.1 mA cm^{-2} at 1.23 V *vs.* RHE was obtained with a W-doped $BiVO_4$ photoanode on titanium felts under simulated sunlight using a 0.1 M Na_2SO_4 aqueous solution. A transparent porous conductive substrate made of interconnected SiO_2 fibres coated with fluorine-doped tin oxide (FTO) was tested with different semiconducting materials in contact with a proton-exchange ionomer.[21] Using transparent conductive substrates, a tandem photoanode-photocathode MPEA may be developed properly tuning the bandgaps of the two materials to utilise a larger fraction of the solar spectrum.[22] Anion exchange ionomers were used to integrate photoelectrodes made of TiO_2 or hematite (α-Fe_2O_3).[23,24]

The MPEA review by Amano *et al.*[25] describes the synthesis of photoelectrodes, their integration in an assembly with solid ionomers and their performance characterization using water in liquid or gas phase. However, there is still limited information on the effects of (photo)corrosion of the semiconductor or of the co-catalysts in this device configuration. Understanding the mechanism and the effects of the degradation phenomena is crucial to cover the stability gap for technologically viable PEC water splitting.[26]

The majority MPEAs were tested at ambient conditions. Operation of PEC devices at higher temperature may affect light absorption, charge separation and recombination as well as water splitting and (photo)corrosion reaction rates.[27] The effects of temperature in MPEAs need clarification. Mass transport of water from the channel to the surface of the photoelectrode may be affected by the flow field geometry of the cell, especially if humid air is used as the reactant. Mass transport limitations caused by non-homogeneous relative humidity in the cell have to be avoided while minimizing the pressure drop in the device. This trade-off has been studied in depth for proton-exchange[28,29] and anion-exchange electrolysis[30] but it has never been addressed for MPEAs.

In this work, the performance and stability of MPEAs for solar water splitting with a Mo-doped $BiVO_4$ (Mo:$BiVO_4$) photoanode and a cobalt phosphate (CoPi) co-catalyst on titanium or stainless steel (SS) felts were assessed. $BiVO_4$ was selected as a reference material to investigate the effects of the (photo)corrosion in MPEAs as it is a promising semiconductor for PEC water splitting and the mechanism of (photo)corrosion in liquid electrolyte has already been investigated.[31–36] CoPi is an efficient co-catalyst for $BiVO_4$ as it acts as passivation layer which suppresses surface recombination of photogenerated minority carriers.[37]

The fabrication of the photoelectrodes on metallic felts was first optimized evaluating the photoelectrochemical performance in a liquid electrolyte. The optimized samples were then integrated in proton-exchange or anion-exchange MPEAs. Their performance and stability were assessed under simulated solar light using liquid water at 30 °C, 43 °C or 56 °C to evaluate for the first time the effects of temperature in MPEAs (Table S1). The effects of (photo)corrosion reactions were evaluated before and after the PEC tests with liquid water by detailed material (photoabsorber, co-catalyst, membrane, etc.) and reactant/product analysis (via SEM, ICP-MS, XPS, etc.). Finally, vapour-phase water splitting in proton-exchange MPEAs was demonstrated at 30 °C. Their performance and stability were assessed with two different flow field configurations to evaluate their impact on the vapour mass transport.

2 Experimental

2.1 Fabrication of $BiVO_4$ photoanodes

The simplified successive ionic layer adsorption and reaction (s-SILAR) procedure to prepare Mo:$BiVO_4$ photoanodes on metallic felts was adapted from literature.[19] We used either titanium felts (porosity 72%, thickness 250 μm, Fuel Cell Store) or stainless steel (SS) felts (porosity 82%, thickness 500 μm, Bekaert), which were cleaned through three successive ultrasonic rinsing steps in acetone, ethanol and water. The felts were cut into 2 × 2 cm^2 pieces and then covered with PVC tape leaving an uncovered area of 3.6 cm^2 on one of the two sides. This PVC-tape mask followed the shape of the flow field geometry used (straight, single serpentine, or interdigitated) to guarantee the direct contact between the flow field/current collector plate and the uncoated felts. The Bi-precursor solution was 40 mL of 0.025 M $Bi(NO_3)_3 \cdot 5H_2O$ in water and acetic acid in 19:1 volumetric ratio. The V-precursor solution was 40 mL of 0.025 M NH_4VO_3 in water. Mo-doped samples were obtained by substituting 1%, 3% or 5% in moles of NH_4VO_3 with $(NH_4)_2MoO_4$ to keep a 1:1 molar ratio of Bi/(V+W) in the two solutions (to theoretically obtain $BiV_{0.97}Mo_{0.03}O_4$). A single s-SILAR cycle consisted in immersing the masked felt in the Bi-

View Article Online
DOI: 10.1039/D6SE00417B

precursor solution for 30 s and then in the V-precursor solution for other 30 s with intervals of 60 s between each immersion to dry the felt under flowing N_2. After the removal of the tape mask, the samples were annealed in a muffle furnace (Carbolite Gero) at 550 °C for 2 h with a heating rate of 2.5 °C min^{-1}. Afterwards, the coated felts were immersed in a 1 M KOH aqueous solution for 20 minutes (to remove the unreacted and excess vanadium), rinsed with water and dried in air. The Mo:$BiVO_4$ samples were finally annealed in a retorted furnace (Carbolite Gero) at 300 °C for 10 minutes using a 5 °C min^{-1} ramp rate with a flow of 500 mL min^{-1} of a mixture 5% H_2/ 95% N_2. This mild heat treatment in a reductive hydrogen atmosphere was used to improve the carriers mobility and lifetime in Mo:$BiVO_4$.[38]

2.2 CoPi co-catalyst photoelectrodeposition

The procedure for CoPi photoelectrodeposition on Mo:$BiVO_4$ photoanodes was adapted from literature[39] to preferentially deposit the co-catalyst on the most photoactive sites of the semiconductor surface (*i.e.* the exposed surface of the semiconductor). A Mo:$BiVO_4$ on metallic felt (working electrode), a reversible hydrogen electrode (Gaskatel Hydroflex), and a graphite rod (counter electrode) were immersed in an electrolyte of 0.5 mM $Co(NO_3)_2 \cdot 6H_2O$ and 0.1 M potassium phosphate solution with pH ≈ 7 (molar concentration ratio KH_2PO_4 : K_2HPO_4 of 1.63:1). Using a methodology previously described,[40] the samples were placed at a distance of 106 mm from a blue LED (ILS OSLON SSL4, peak wavelength 442 nm, 173 ± 7 W m^{-2} at 106 mm) to simulate the useful irradiation absorbed from the AM 1.5G spectrum. The LED was powered by constant-current LED drivers (0.7 A, ILS IZC070) and attached to an aluminium heat sink by thermal adhesive. A simplified schematics of the setup is shown in Fig. Figure S1. A constant potential of 1.0 V *vs.* RHE was applied for 20 minutes using a Biologic VSP potentiostat.

2.3 Preliminary PEC tests for photoanodes optimization

The Mo dopant molar concentration, total semiconductor loading, and CoPi catalyst deposition was optimized by varying the number of s-SILAR cycles and concentration of precursors in order to maximize the photoelectrochemical performance. The PEC measurements were performed in a beaker with 200 mL of a 0.2 M Na_2SO_4 aqueous solution and the same setup shown in Fig. Figure S1 was used. Cyclic voltammetries (CVs) between 0.2 and 1.6 V *vs.* RHE at a scan rate of 10 mV s^{-1} were performed, reporting the average of the third forward sweeps of the CV of two different coated felts. The high-frequency resistance (HFR) was obtained fitting the electrochemical impedance spectroscopy imposing a sinusoidal wave with amplitude of 20 mV and a frequency of 50 kHz at a constant potential of 1.23 V *vs.* RHE. Where specified, 0.1 M of Na_2SO_3 was added to the electrolyte as hole scavenger. The catalytic efficiency η_{cat} was used as a performance indicator as previously proposed by Dotan *et al.*[41] (Eq. 1).

$$\eta_{cat} = \frac{j_{H_2O}}{j_{Na_2SO_3}} \quad (1)$$

j_{H_2O} is the current density resulting from an experiment without hole-scavenger (i.e. oxygen evolution reaction will dominate) and $j_{Na_2SO_3}$ is the current density measured with a hole scavenger, Na_2SO_3, assuming that all photogenerated holes reaching the surface of the photoelectrode contribute to the sulfite anion oxidation without recombination.

2.4 Membrane-photoelectrode assembly preparation

The proton-exchange ionomer dispersion was obtained using Nafion™ ionomer pellets, ethanol and deionized water in 18.5:80:1.5 mass proportion. For the anion-exchange ionomer, Fumion™ FAA-3 shredded films and 1-propanol in 25:75 mass proportion were used. Layers of proton-exchange and anion-exchange ionomer inks, with thicknesses of 300 μm and 650 μm respectively, were obtained through a doctor blade method. The coated Ti felts were placed in the proton-exchange ionomer layer leaving the semiconductor side on top. For the coated SS felts, the semiconductor side was pointing downwards when placing them in the anion-exchange ionomer layer. The samples were dried in ambient air for 30 minutes to let the solvents evaporate. The excess ionomer was cut away from the dry layers to obtain the ionomer-coated felts. Nafion™ 115 proton-exchange membranes (PEM, thickness 127 μm) coated with a Pt/C cathode catalyst layer (catalyst loading 0.08 mg cm^{-2}, Johnson Matthey) and Fumasep™ FAA-3-50 anion-exchange membranes (AEM, thickness 50 μm) coated with a Pt/C layer (catalyst loading 0.4 mg cm^{-2}, Johnson Matthey) were used for the membrane-cathode assemblies. To obtain a membrane-photoelectrode assembly, the ionomer-coated felts were placed on top of the catalyst-coated membrane with the semiconductor side pointing upwards and in between some PTFE gaskets. Hot pressing for 2 minutes at 150 °C for proton-exchange membrane (PEM) or at 80 °C for anion-exchange membrane (AEM) was performed without applying any pressure, *i.e.* the plates were only touching the two external gaskets without any air gap in between, not to risk to compress too much and to damage the coated porous layer. A simplified schematic of the steps to prepare the membrane-photoelectrode assemblies is shown in Fig. Figure S2.

2.5 Photo-electrolyzer cell design

Inspired by low-temperature electrolyzers, a cell to test membrane-photoelectrode assemblies was designed and is henceforth referred to as the *photo-electrolyzer* (Fig. 1(a)). A quartz window and a PVC gasket transparent in the visible region allowed to illuminate the photoanode integrated in the MPEA. A carbon porous transport layer (Sigracet 39AA, 280 μm thickness, 80% porosity, Fuel Cell Store) was used at the cathode side. Titanium flow fields with straight, single serpentine or interdigitated geometry were also the current collectors in contact with the porous conductive layers. PEEK external plates and PTFE gaskets completed the cell, avoiding leakages.

2.6 Introduction of the external reference electrode

An external reference electrode was introduced in the photoelectrolyzer in an edge-type configuration taking inspiration from previously proposed methodologies.[42–44] A hydrogen reference

View Article Online
DOI: 10.1039/D6SE00417B

electrode (Gaskatel Hydroflex) was placed outside the cell and immersed in a 1 M H_2SO_4 aqueous solution for PEM experiments. The solution was ionically connected to the membrane through a Nafion™ tube (0.84 mm OD, Fuel Cell Store) in a PTFE tubing (0.9 mm OD) filled with a 1 M H_2SO_4 aqueous solution. A 1 M NaOH aqueous solution was alternatively used for the AEM experiments. The PTFE tube was inserted in a Fidex F-130X fitting and inserted in the photo-electrolyzer cathodic PEEK plate to avoid leakages. The schematic representation of the system is shown in Fig. 1(b). The applied potentials *vs.* RHE were not corrected for the ohmic drop in the membrane given the low operating current densities. The Donnan potential at the membrane-liquid electrolyte interface was assumed negligible.

2.7 Setup for the tests with liquid water or humid air

Liquid deionized water (200 mL) was stored in glass bottles and it was sent to both sides of the photo-electrolyzer using a multichannel Shenchen LabV1 peristaltic pump with a MC12 pump head. A water volumetric flow rate of 13 mL min^{-1} was imposed. The glass bottles were placed in a 28 L water bath (Fisherbrand Isotemp) to control the temperature of the working fluid. Tests with water in vapour phase were performed imposing a flow of nitrogen to pass through a humidifier before reaching the photo-electrolyzer. Nitrogen volumetric flow rates from 20 to 220 mL min^{-1} in both compartments of the cell were imposed through mass flow controllers (Bronkhorst F-201CV). The temperature in the cell was measured using K-type thermocouples connected to a Pico Technology TC-08 data logger. The thermocouples were introduced into a port of each flow field plate to obtain an estimate of the operating temperature of the electrodes. The photo-electrolyzer was illuminated by AM 1.5G simulated irradiation from a Trisol Solar Simulator (AOI) calibrated with an Ocean Insight FLAME-S-XR1 spectrometer (optical resolution 1.7 nm FWHM) connected to an optical fibre (core diameter 300 μm, length 1 m) and a cosine corrector (CC-3-UV-S, OceanInsight). The schematic representation of the two setup configurations is reported in Fig. Figure S3 - Figure S4.

2.8 PEC characterization of the membrane-photoelectrode assemblies

The membrane-photoelectrode assemblies were characterized in three-electrode configuration connecting the anodic metallic plate of the photo-electrolyzer to the working electrode, the cathodic plate to the counter electrode and using the external hydrogen electrode as reference (Fig. 1(b)). The external reference electrode used was considered as a reversible hydrogen electrode (RHE) as in previous reports.[42,45] The current density-potential characteristic curves of proton-exchange MPEAs were obtained applying potentials from 0.7 to 1.6 V *vs.* RHE for 60 s. Similar curves were obtained for the anion-exchange MPEAs applying potentials from 0.7 to 1.3 V *vs.* RHE for 60 s as a dark current associated to the oxidation of the SS felt was observed for larger potentials.[46] The current densities reported in the characteristic curves are the averages of the steady state values of two different samples. All the error bars reported were obtained from the standard deviation of the measurements of two samples. Chronoamperometric measurements imposing 1.23 V *vs.* RHE were interspersed with current density-potential characteristic curves. Tests with liquid water at 30 °C, 43 °C and 56 °C were performed, only tests at 30 °C were performed with water vapour. The onset potential was defined as the potential *vs.* RHE measured at 0.02 mA cm^{-2} and it was calculated with a linear interpolation of the experimental points. The saturation current density was defined as the average current density measured at 1.2 V *vs.* RHE in the characteristic curves.

Photostability was analysed by extracting 10 mL of liquid water from the anodic reservoir after two current density-potential characterizations performed after different time spans of chronoamperometry. The chemical stability of the samples was analysed leaving both the proton-exchange or anion-exchange MPEAs, both the metallic felts (Ti and SS) coated with Mo:$BiVO_4$ and CoPi (without ionomer), or the annealed SS felts (without any coating), either in liquid water, in a 0.005 M H_2SO_4 aqueous solution (pH ≈ 2) or in a 0.01 M NaOH aqueous solution (pH ≈ 12). Liquid samples were then analysed using inductively coupled plasma mass spectroscopy (ICP-MS, Agilent Technologies LC Infinity II Triple Quad 8900) to quantify the amount of dissolved elements.

2.9 Material characterization

The Mo:$BiVO_4$ coated felts and the MPEAs were observed before and after operation using scanning electron microscopy (SEM). Jeol JSM-IT300 SEM operating at 20 kV was used for pristine samples, Zeiss GeminiSEM 300 working at 3 kV for aged samples. For the cross-section SEM images of pristine MPEAs, the samples were embedded in epoxy resin and mechanically polished after solidification until obtaining a mirror-like surface. For the aged samples, the membranes were broken in two pieces in liquid nitrogen to obtain a sharp rupture. A carbon deposition pre-treatment was performed before every cross-section SEM observation. The nanostructures of Mo:$BiVO_4$ were mechanically scratched away from the metallic felts with a razor blade and deposited on a standard Cu grid. They were then observed by transmission electron microscopy (TEM, Tecnai Osiris operated at 200 kV) and energy-dispersive X-ray spectroscopy (EDXS). Anion-exchange membranes after the PEC tests with liquid water at 30 °C were embedded in epoxy and cut by ultra-microtomy into 90 nm lamellas and put on CF200-CU-50 grids for TEM and EDXS measurements.

The elemental surface composition of the samples was evaluated by X-ray photoelectron spectroscopy (XPS). The synthesis steps from $BiVO_4$ to Mo:$BiVO_4$ with CoPi on Ti felt were analysed using a Thermo Nexsa instrument, while the effects of photocorrosion were investigated using a Kratos AXIS Supra. The binding energies were corrected with reference to adventitious C 1s peak at 284.8 eV and normalized separately for the samples measured with each instrument.

Spectral hemispherical reflectance and transmittance spectra of Mo:$BiVO_4$ on titanium and SS felts or on a planar FTO-coated glass substrate were measured with a Shimadzu UV-2600 UV-

View Article Online
DOI: 10.1039/D6SE00417B

vis-NIR spectrophotometer with an integrating sphere (ISR-2600 PLUS Shimadzu). Absorption spectra were calculated from these data. The Tauc plot was fitted assuming an indirect optical transition to obtain the optical bandgap of the semiconductor at ambient temperature[47]. A correction for a baseline of the absorbing metallic felts was applied as previously proposed.[48] The transmittance of a thin layer of proton-exchange thin layer (10 μm) and anion-exchange (60 μm) ionomer on FTO-coated glass were obtained following the same methodology.

3 Results and Discussion

3.1 Optimization and characterization of the photoanodes

In order to maximize the MPEA performance, the concentration of Mo dopant and the number of s-SILAR cycles were optimized. Mo acts as an electron donor in the $BiVO_4$ lattice.[49] The optimal molar concentration of Mo dopant was found to be 3% (Fig. Figure S5). Lower Mo concentrations seem to not provide enough free electrons in the lattice whereas too large Mo concentrations reduce the space charge region thickness and may induce lattice strain or even the formation of Mo oxides and defects, acting as recombination centres.[50] The optimal number of s-SILAR cycles for Mo:$BiVO_4$ on titanium and stainless steel felts was found to be 8 and 6 respectively (Fig. Figure S6 and Figure S7 (c)-(d)). A current density of 0.57 and 0.69 mA cm^{-2} was achieved at 1.23 V *vs.* RHE with the Ti and SS substrates, respectively. SS felts also allowed for a better extraction of photogenerated charges at lower potentials. For a lower number of s-SILAR cycles, the small amount of semiconductor on the felt leads to reduced light absorption[51] (Fig. Figure S7 (a)-(b)). The high-frequency resistance (HFR) of the samples did not vary when increasing the number of cycles above the optimum (12 Ω cm^2 for Mo:$BiVO_4$ on Ti felts and 20 Ω cm^2 for the semiconductor on SS felts for more cycles than the optimal one), excluding ohmic losses as explanation. Likely, a larger amount of the generated charge carriers is further away from the interface and charge extraction becomes more difficult. This optimal Mo concentration and number of s-SILAR cycles was fixed for all of the subsequent experiments.

For the optimal number of s-SILAR cycles, the Mo:$BiVO_4$ semiconductor nearly completely covers the fibres of both the Ti and SS felts (Fig. 2 (a)-(b)). The semiconductor formed nanostructures on the fibres (Fig. 2 (c) andFigure S8), increasing the specific surface area for the anodic reaction. Nanostructures also ensure the collection of photogenerated minority charge carriers perpendicular to the direction of light absorption, which is beneficial considering the short diffusion length of doped $BiVO_4$ photoanodes (between 50 and 100 nm)[52,53]. After the photoelectrodeposition of CoPi, the co-catalyst formed a layer of approximately 30 nm on Mo:$BiVO_4$, helping to suppress the surface recombination at the interface with the electrolyte[37] without considerably compromising the light absorption (Fig. 2 (d)-(e)-(f) and Figure S9). The indirect optical bandgap of the semiconductor was measured to be 2.47 eV (Fig. Figure S10), in agreement with values around 2.4-2.5 eV previously reported.[47]

The surface composition and electronic structure of the photoanodes were analysed by XPS. Pristine $BiVO_4$ and Mo:$BiVO_4$ with CoPi, both on Ti felts, were initially studied (Fig. 3). For the pristine $BiVO_4$ on Ti, the Bi spectrum exhibited two peaks at binding energy levels of 159.2 eV and 164.5 eV, which correspond to the Bi $4f_{7/2}$ and Bi $4f_{5/2}$ of Bi 4f levels, attributed to the presence of Bi(III) state at the surface of the film.[54] The peak at 516.9 eV was ascribed to the V $2p_{3/2}$ state of V(V) oxidation state.[19] The deconvolution of the O 1s spectrum shows two peaks at 530.0 eV and at 531.7 eV, which were attributed to the oxygen in the lattice and the chemisorbed or dissociated oxygen from water molecules.[54] The comparison between the spectra of the pristine $BiVO_4$ and the ones of Mo:$BiVO_4$ with CoPi reveals shifts in the binding energy of the peaks and the variation of their intensities, indicative of strong interactions between the co-catalyst, the semiconductor and the supporting material.[55] The XPS peaks of Bi 4f and V 2p in Mo:$BiVO_4$ with CoPi slightly shifted to lower binding energies and decreased in intensity compared to the pristine material without co-catalyst. These shifts suggest charge redistribution and possible catalyst-semiconductor interfacial effects, which can play a critical role in the catalytic performance of the system. The reduction of the intensity of the peaks of Bi and V is in agreement with the TEM results where a conformal layer of CoPi was observed over $BiVO_4$ (Fig. 2 (e)-(f)). Indeed, similar results have been previously reported in studies examining the surface coverage of co-catalysts on different supports.[56,57] The O 1s spectrum exhibits noticeable broadening and different peak positions upon the co-catalyst deposition. The peaks observed at 529.4 eV, 531.4 eV and 530.8 eV can be deconvoluted into three curves related to lattice oxygen, oxygen vacancy and absorbed OH groups.[58–60] The appearance of the Mo $3d_{5/2}$ peak at 232.5 eV confirmed the presence of the Mo dopant in the $BiVO_4$ lattice.[61] However, a minor contribution of Mo was also found in the pristine material, and it was attributed to its presence in traces in the commercial metallic substrate used. After the photo-electrodeposition of CoPi, Co $2p_{3/2}$ and Co $2p_{1/2}$ peaks were detected at 780.9 eV and 796.7 eV, respectively. These peaks were attributed to the Co(II)/Co(III) oxidation states of cobalt, as previously observed for CoPi. Additional peaks of Co 2p were attributed to the formation of Co-O and Co-O-P interactions.[55,62] The peak at 133.4 eV in the P 2p region is derived from the phosphate, confirming the formation of CoPi on the photo-electrode surface.[54] Fig. Figure S11 presents the XPS spectra of the as-prepared $BiVO_4$ and Mo:$BiVO_4$ with CoPi samples on stainless steel felts. With the different substrate, the chemical elements and their oxidation states were the same as observed using Ti felts. The main differences were attributed to using stainless steel as metallic support. The presence of Bi, O, Mo, Co, and P species in the metal alloy was confirmed by the XPS peaks of the annealed stainless steel felts (Fig. Figure S12).

Testing the samples on Ti felts in a 0.2 M Na_2SO_4 aqueous solution, the reduction of ohmic losses with the introduction of Mo dopant and the improvement in the extraction of photogenerated holes with CoPi co-catalyst can be noticed (Figure S13). A current density of 1.5 mA cm^{-2} was obtained at 1.23 V *vs.* RHE at 30 °C in the optimal configuration. This current is smaller than the maximum photocurrent density obtained with nanostructured planar $BiVO_4$ substrates of 7.15 and 7.0 mA cm^{-2} at 1.23 V *vs.* RHE under AM 1.5G illumination respectively obtained by Zhao et al.[63]

View Article Online
DOI: 10.1039/D6SE00417B

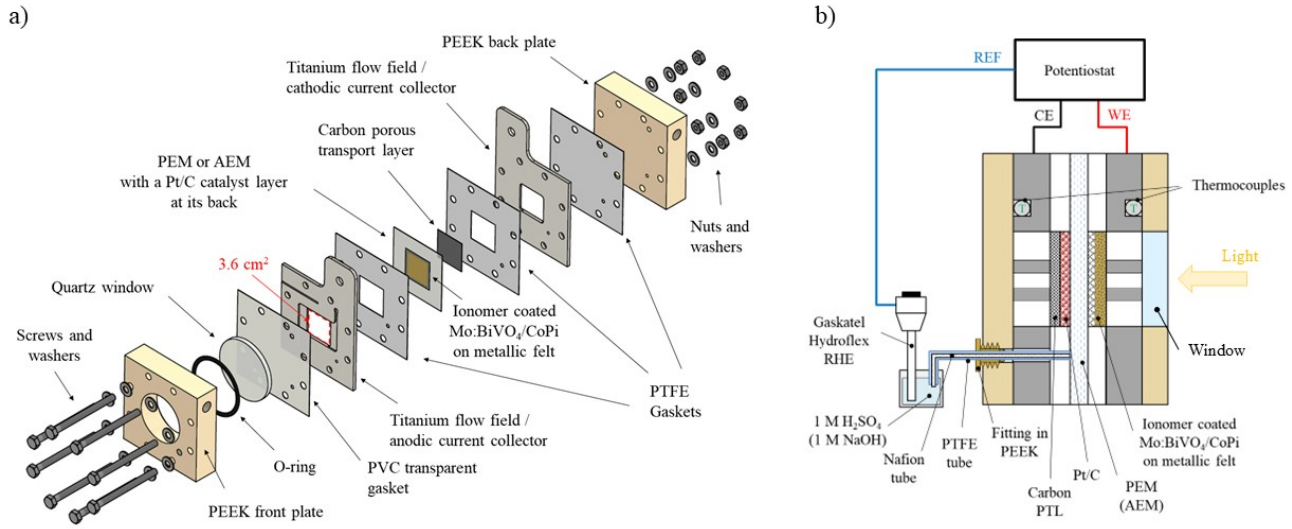

Fig. 1 (a) Exploded view of the photo-electrolyzer cell; (b) schematic representation of the proton-exchange system to introduce the external hydrogen reference electrode in an edge-type configuration.

and Liu *et al.*[64] Despite being still far from the maximum theoretical limit of 7.5 mA cm^{-2}, the performance in Na_2SO_4 electrolyte reported here is similar to the one of other $BiVO_4$ photoanodes on porous substrates previously reviewed by Zafeiropoulos *et al.*[19] After the photoelectrochemical deposition of CoPi on Mo:$BiVO_4$ on Ti felts, the catalytic efficiency η_{cat} of the samples increased from 17% to 62% at 0.8 V *vs.* RHE. In dark, the oxidation of Na_2SO_3 determined a dark current density with an onset potential at approximately 0.9 V *vs.* RHE which did not allow to calculate the catalytic efficiency η_{cat} for larger potentials.

3.2 Membrane-photoelectrode assemblies

After the deposition of the ionomers and the evaporation of the solvent, the polymer conformally coated the metallic fibres and the nanostructures of Mo:$BiVO_4$ with CoPi (Fig. 4 (a) and Figure S14). The doctor blade technique facilitated a strategically non-uniform deposition of ionomer throughout the thickness of the felts (Fig. Figure S15). The ionomer only covered the fibres of the felts and the semiconductor nanostructures on the side directly exposed to light, which ensured the electrolytic contact with the photoactive particles and optimal mass transfer of the reactant to the surface of the photoelectrode. The proton-exchange ionomer is almost transparent for wavelengths smaller than the one characteristic to the bandgap of $BiVO_4$ (Fig. Figure S16). The anion-exchange ionomer reduces its transmittance in the UV region, which may penalize the generation of charges in the semiconductor. On the opposite side in contact with the membrane, the ionomer filled the pores among the fibres to guarantee a better adhesion to the membrane. The hot press treatment resulted in the integration of the felts in the membrane-photoelectrode assemblies with the Pt/C cathode catalyst layers (Fig. 4 (b)-(c)-(d)). The use of PVC tape to mask areas where s-SILAR deposition is undesirable enabled the creation of MPEAs which follow the shape of the flow field plate used. This avoids contact between the semiconductor-coated felt and the metal plate contact, which would unfavourably increase contact resistance (although a thin layer of metal oxide may have formed in those regions during the annealing process). Furthermore, preventing the deposition on the non-illuminated electrode area minimizes the wasted photoactive and catalyst materials and optimizes their loading on the felt (Fig. 4 (e)).

3.3 PEC characterizations with liquid water

The proton-exchange and anion-exchange MPEAs were initially tested at various temperatures using liquid-phase water. For pristine proton-exchange MPEAs, an increase in the onset potential with temperature increase was observed: 0.77 V *vs.* RHE at 30 °C to 0.83 V *vs.* RHE at 56 °C, with an average rate of +3.7 mV K^{-1} (Fig. 5 (a)). The onset potential difference in light and dark decreased with increasing temperature, primarily due to a more pronounced surface recombination of photogenerated minority carriers compared to their transfer to the electrolyte, as previously observed for tin-doped hematite photoanodes.[40] The saturation current density increased from 0.30 mA cm^{-2} at 30 °C to 0.40 mA cm^{-2} at 56 °C (average rate +0.62 μA cm^{-2} K^{-1}), following a trend in agreement with previous reports about $BiVO_4$ thin films.[61,65] We expect the bandgap of the semiconductor to decrease with temperature as described by the Varshni model[66] by approximately 8 meV.[67] This decrease corresponds to a 1.2% larger photon flux with energy greater than the bandgap. The spectral absorption coefficient at photon wavelengths smaller than the absorption edge to increase with temperature. The increased absorption of photons combined with a better kinetics of the electrochemical oxidation is expected to lead to a higher saturation current density with increasing temperature.

The pristine anion-exchange MPEAs at 30 °C had an onset potential of 0.81 V *vs.* RHE (Fig. 5 (b)), which is comparable to the ones obtained with proton-exchange MPEAs. However, lower photocurrent densities were observed, especially at low applied potentials. At 1 V *vs.* RHE and 30 °C, anion-exchange MPEAs

View Article Online
DOI: 10.1039/D6SE00417B

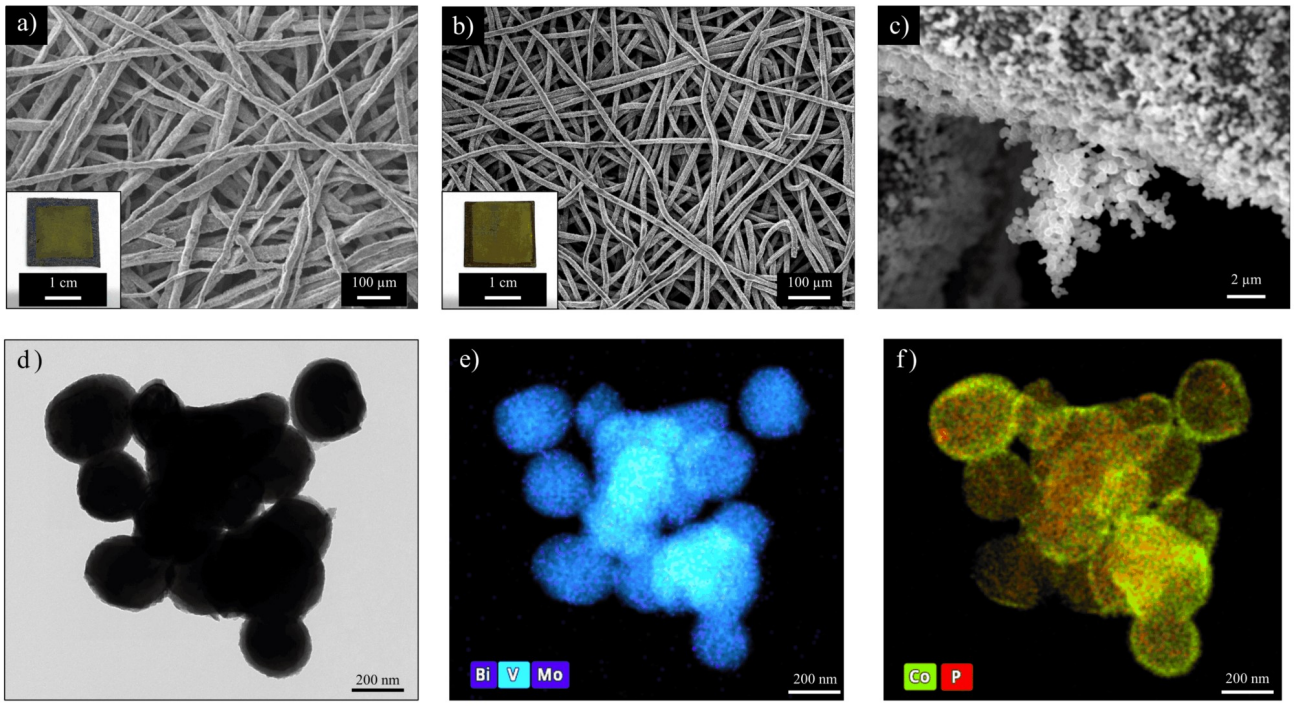

Fig. 2 (a) SEM image and photograph of Mo:$BiVO_4$ on Ti felt after 8 s-SILAR cycles; (b) SEM image and photograph of Mo:$BiVO_4$ on stainless steel felt after 6 s-SILAR cycles; (c) SEM image of a nanostructure of Mo:$BiVO_4$ formed on a Ti fibre; (d) TEM image of a Mo:$BiVO_4$ with CoPi nanostructure scratched off a metallic felt; (e)-(f) EDXS elemental mapping of (e) Bi, V and Mo and (f) Co and P of the same nanostructure.

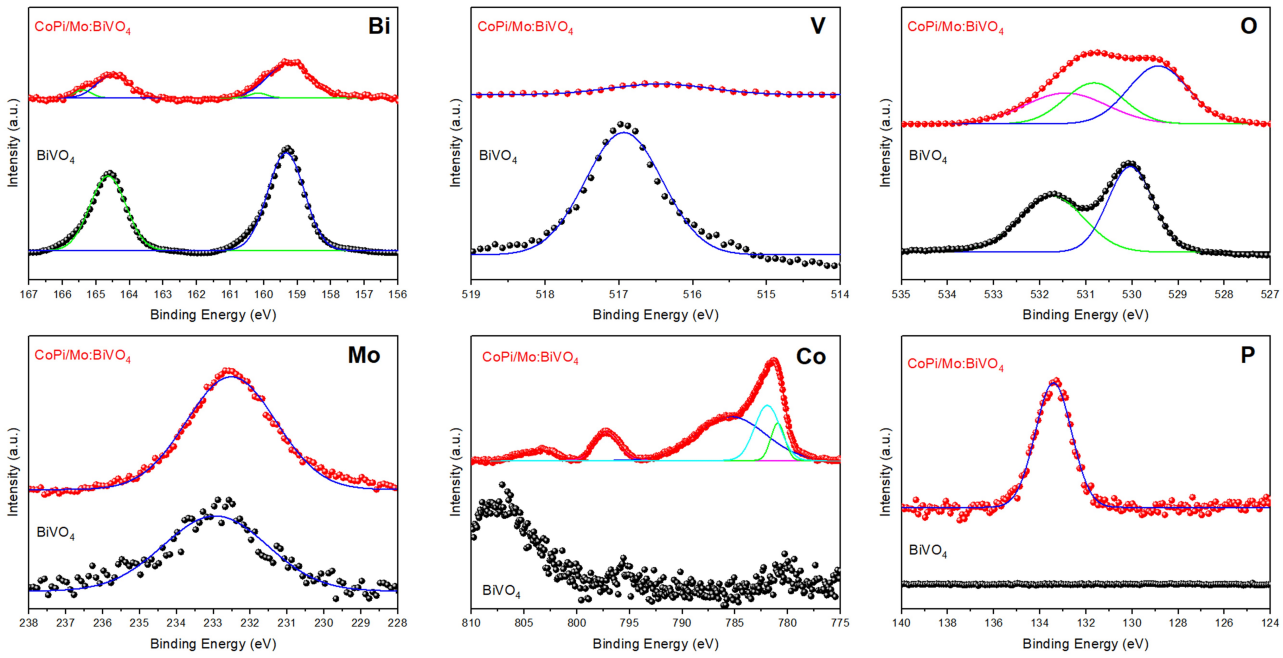

Fig. 3 XPS spectra of pristine $BiVO_4$ (black dots) and Mo:$BiVO_4$ with CoPi (red dots) on titanium felt with the corresponding Lorentzian deconvolution for data fitting (lines) in the binding energy ranges for Bi, V, O, Mo, Co and P.

View Article Online
DOI: 10.1039/D6SE00417B

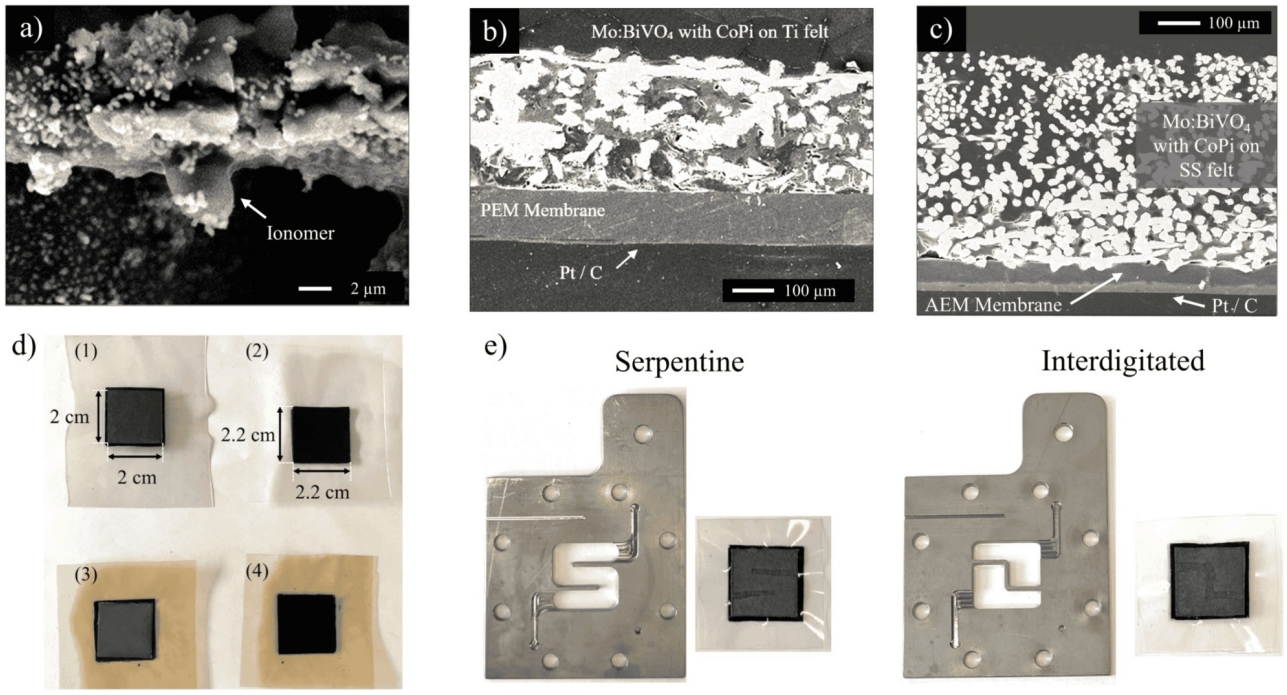

Fig. 4 (a) SEM image of the Mo:$BiVO_4$ nanostructures on a Ti fibre covered by proton-exchange ionomer; (b) cross-section SEM images of the proton-exchange membrane-photoelectrode assembly after the hot press treatment; (c) cross-section SEM image of an anion-exchange MPEA after the hot press treatment; (d) photograph of the proton-exchange (or anion-exchange at the bottom) membrane-photoelectrode assemblies: (1)/(3) from the photoanode side or (2)/(4) from the Pt/C cathode catalyst layer side; (e) photograph of the serpentine and interdigitated flow field plates with the proton-exchange MPEAs with the selective deposition of the Mo:$BiVO_4$ to follow their shape.

generated a current density of only 0.06 mA cm^{-2}, compared to 0.23 mA cm^{-2} with proton-exchange MPEAs under identical conditions. A less efficient charge extraction at the photoanode-electrolyte junction may explain this loss of current at larger applied potentials, further widening the performance gap with respect to the best performing nanostructured photoelectrodes on planar FTO-coated glass.[63,64] Fumion™ FAA-3 ionomer partially absorbs light in the visible spectrum and mainly in the UV, as reported in Fig. Figure S15. Its thickness in the order of hundreds of nm on the photoanode surface is expected not to significantly penalize light absorption in the semiconductor. The onset potential difference in light and dark and photocurrent density produced by the anion-exchange MPEAs decreased further when operating at 56 °C.

Next, the behaviour of both proton-exchange and anion-exchange MPEAs was assessed after operating for a number of hours. After applying a potential of 1.23 V *vs.* RHE for 4 hours at 30 °C (Fig. Figure S17 (a)), both the saturation photocurrent density and onset potential difference produced in anion-exchange MPEAs decreased over time (Fig. 5 (c)). Applying the same potential to the proton-exchange MPEAs, a decrease of the saturation current density in time was also observed for samples tested at 56 °C and 43 °C (Fig. 5 (d)-(e)). A larger drop of current density was observed in the first hour of test with a slower subsequent decrease (Fig. Figure S17 (b)). The chemical and photoelectrochemical corrosion of $BiVO_4$ in acidic environment followed by the dissolution of the produced species may reduce the amount of photoactive semiconductor in time,[35] decreasing the amount of light collected and therefore the saturation photocurrent density. During the tests at 30 °C, the saturation current density was not affected by the application of 1.23 V *vs.* RHE for 15 hours (Fig. 5 (f)). The same trends at different temperatures were also observed during chronoamperometry (Fig. Figure S17 (b)): the average reduction of the current density in time at 56 °C was −8.6 μA cm^{-2} h^{-1} while it was negligible at 30 °C. The almost constant photocurrent density at 30 °C for 15 h does not imply a perfect stability of the samples, long-term tests (up to thousands of hours) have to be performed to fully evaluate the impact of photocorrosion. The negative currents measured are associated to reduction reactions as previously observed by Zafeiropoulos *et al.*[19]. Their exact nature was not determined but could be associated to the residual oxygen reduction on the uncoated Ti surface, the reduction of TiO_2, other oxides or cobalt in CoPi.

3.4 Photocorrosion in proton-exchange MPEAs after tests with liquid water

ICP-MS measurements were used to quantify the amount of various elements in the liquid water and thereby evaluate the photocorrosion of Mo:$BiVO_4$ photoanodes with CoPi co-catalyst during operation. Following the tests with proton-exchange MPEAs, the liquid water of the anodic reservoir contained more vanadium than bismuth (Fig. 6), with a difference in moles of almost two orders of magnitude (N''_{V,H_2O}(5 h, 30 °C) = 62.2 nmol cm^{-2} versus N''_{Bi,H_2O}(5 h, 30 °C) = 0.65 nmol cm^{-2}). From the Pourbaix diagram of $BiVO_4$, BiO^+ and VO_4^- are predicted to be produced

View Article Online
DOI: 10.1039/D6SE00417B

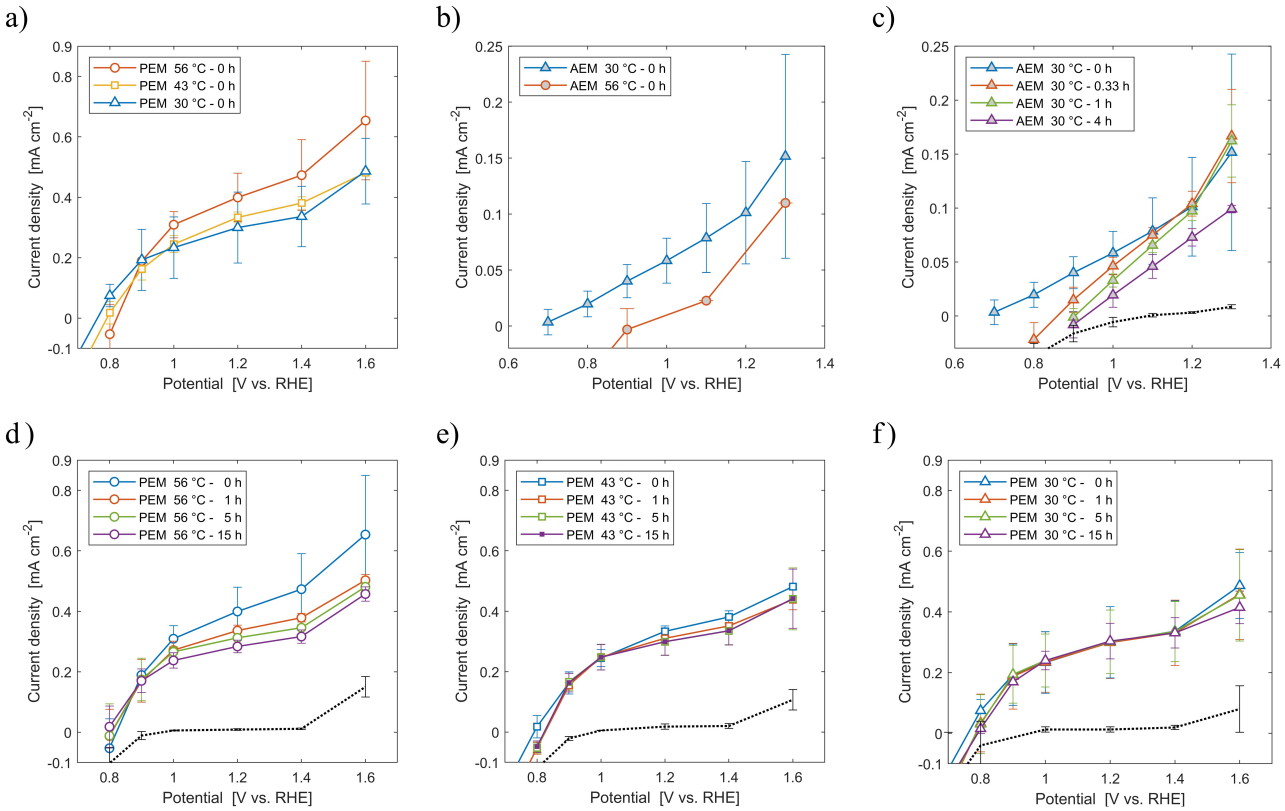

Fig. 5 (a)-(b) Current density-potential characteristic curves with liquid water at different temperatures of pristine (a) proton-exchange MPEAs, and (b) anion-exchange MPEAs. (c) Current density-potential characteristic curves of anion-exchange MPEAs after different duration of exposure to chronoamperometry at 1.23 V *vs.* RHE with liquid water at 30 °C. (d)-(e)-(f) Current density-potential characteristic curves of proton-exchange MPEAs after different duration of exposure to chronoamperometry at 1.23 V *vs.* RHE with liquid water at: (d) 56 °C, (e) 43 °C, (f) 30 °C. The black dotted lines in the figure represent the characteristic curves with liquid water of the pristine MPEAs in dark.

from the photocorrosion of the material in mildly acidic environment and under high potential.[31] The lower concentration of bismuth may be caused by the transfer of the produced BiO^+ to the cathodic water reservoir through the proton-exchange membrane and the repulsion towards the anodic reservoir of VO_4^- from the negative sulfonic groups of the Nafion™ ionomer. A more complex mechanism governing selective vanadium dissolution, as observed by Lee and Choi[32], could also cause such a difference in concentration. In this case, the dissolution of vanadium from $BiVO_4$ could be reduced through the use of a V^{5+}-saturated electrolyte. At the end of the tests, the amount of Bi measured in liquid water was even less than Mo (N''_{Mo,H_2O}(5 h, 30 °C) = 1.32 nmol cm^{-2}), although the theoretical ratio in the material should be 100:3.

It has previously been shown that the cobalt phosphate is chemically unstable in an acidic environment.[68] Surprisingly, no cobalt was detected in anodic reservoir after the PEC tests with proton-exchange MPEAs, *i.e.* the concentration of Co in water was below the detection limit of 0.05 μg L^{-1}. We hypothesize that the catalyst may therefore have dissolved extremely quickly and may have passed to the cathodic reservoir. The performance in 0.2 M Na_2SO_4 aqueous solution of the pristine proton-exchange MPEA with blue LED light is indeed similar to the one of Mo:$BiVO_4$ on Ti felt without CoPi in liquid water (Figure S18), confirming that the complete dissolution of the thin layer of CoPi may have occurred before the end of this test. Operation at 56 °C accelerates the dissolution of species and the transfer to liquid water without modifying the relative molar ratios between different species observed at 30 °C. Similar trends are observed when comparing photoelectrochemical and chemical dissolution of the species from proton-exchange MPEAs (Fig. Figure S19 (a) to (c)). The applied electrical bias and light increase the quasi-Fermi level of holes in the photoanode *vs.* RHE, accelerating the dissolution of species and their transfer to water without changing the relative molar ratios among the species. However, the dissolution of V and Mo appeared to mainly be chemical rather than photoelectrochemical. Placing a Ti felt coated with Mo:$BiVO_4$ and CoPi (without ionomer) in a 0.005 M H_2SO_4 aqueous solution with pH ≈ 2, the chemical dissolution at 30 °C of Bi, V and Mo followed the theoretical stoichiometric ratios in the material (Fig. Figure S20 (a)). This result confirms that the proton-exchange ionomer may influence not only the transfer of ions but also the photocorrosion mechanism at the photoanode-electrolyte interface. Cobalt was only detected in the chemical stability test with Ti felts coated with Mo:$BiVO_4$ and CoPi (without ionomer) in a 0.005 M H_2SO_4 aqueous solution, confirming the chemical instability of the co-catalyst (Fig. Figure S21 (a)).

Fig. 7 compares the XPS spectra of the pristine Mo:$BiVO_4$ sam-

View Article Online
DOI: 10.1039/D6SE00417B

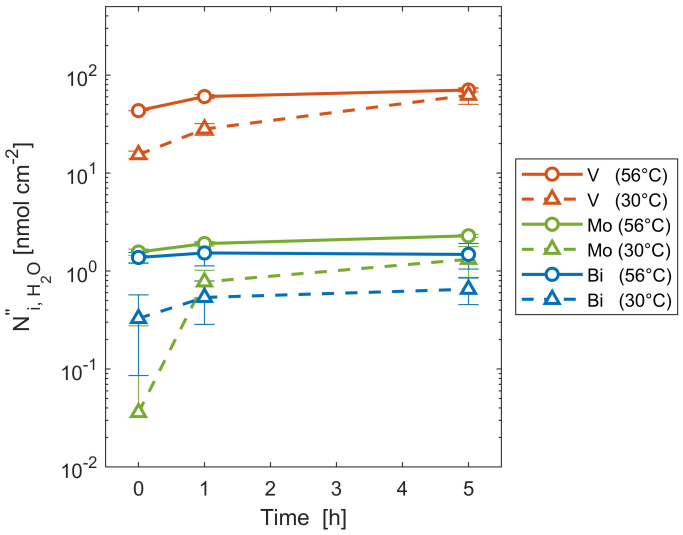

Fig. 6 Moles of Bi, V or Mo dissolved in liquid water per illuminated geometric area of the felts after the chronoamperometry performed at different temperatures with proton-exchange MPEAs. The liquid samples were extracted after two potential-current density characteristic curves with simulated solar light.

ples with CoPi on Ti felt with the ones of the same samples covered by proton-exchange ionomer which were used for the PEC tests with liquid water at 30 °C in MPEA configuration. The two additional contributions to the Bi 4f peaks at 159.9 and 165.2 eV were attributed to Bi_2O_3, which may be a product of the photocorrosion reactions of $BiVO_4$. This conclusion was also supported by the detection of additional features in the O 1s spectrum, which shows a new peak at 529.9 eV attributed to Bi-O bonding and the formation of other oxides.[69] The shift of the V peak from 516.4 eV to 517.6 eV possibly suggests no changes in the oxidation state of V(V), but a different surface interaction with the ionomer. The shift of the peak of Mo $3d_{5/2}$ to a lower binding energy at 231.9 eV suggests a variation of the oxidation state and the possible formation of different species, like molybdenum oxides.[70] The most relevant effect of the PEC tests with liquid water at 30 °C was the total disappearance of Co 2p and P 2p signals, attributed to the complete co-catalyst dissolution.

Examination of the false-colour cross-section SEM images of the proton-exchange membrane after the tests at 56 °C, shown in Fig. 8, reveals that solid particles were formed inside the membrane. These particles coalesced closer to the photoanode, forming clusters of few μm in size (Fig. 8 (a)). Conversely, the characteristic dimension of the particles in the middle of the membrane was in the order of hundreds of nm (Fig. 8 (b)). Analysing the EDXS elemental mapping, the solid particles were mainly composed of vanadium (Fig. 8 (c)). From the Pourbaix diagram of V in water, solid V_2O_5 is predicted to be formed after the complete oxidation of vanadium at low pH and high concentration.[71,72] The solubility of V_2O_5 is extremely low (0.7 mg L^{-1})[73] and its supersaturation in the nanochannels of the proton-exchange membrane has likely happened. Further research is necessary to define the exact mechanism behind the formation of these solid particles in the proton-exchange membrane of the MPEAs. Other solid species containing vanadium (IV) (*e.g.*, V_2O_4) or V (V) (*e.g.*, HVO_3) could possibly have formed. The reactions to form V_2O_5 may have involved the dissolved oxygen or hydrogen in the membrane as already observed for the Pt band formation in proton exchange membrane fuel cells.[74] The identification of the exact mechanism of this phenomenon is not in the scope of this work. Catalyst dissolution followed by the formation and coalescence of solid particles in the membrane has already been observed and modelled in PEM fuel cells[75–77] and electrolyzers[78,79] but it had never been reported for MPEAs.

3.5 Effects of photocorrosion in anion-exchange MPEAs after tests with liquid water

As shown in Fig. 9, after operation of the anion-exchange MPEAs at 30 °C, the concentration of V in the anodic reservoir was more than one order of magnitude larger than the one of Bi (N''_{V,H_2O}(5 h, 30 °C) = 15.5 nmol cm^{-2} versus N''_{Bi,H_2O}(5 h, 30 °C) = 0.58 nmol cm^{-2}). Furthermore, the amount of dissolved Bi detected was less than than that of Mo (N''_{Mo,H_2O}(5 h, 30 °C) = 1.38 nmol cm^{-2}). Operation at 56 °C accelerated the process of dissolution but it also modified the relative amounts of species found in liquid water, more closely following the theoretical stoichiometric ratios of the material. Toma *et al.*[31] proposed that the self-passivation of $BiVO_4$ in alkaline environment with insoluble solid Bi oxides (Bi_4O_7 and Bi_2O_3) is kinetically inhibited despite the predictions from the thermodynamic first-principle calculations. The almost 1:1 molar ratio between bismuth and vanadium we obtained at 56 °C can confirm this theory but this also implies that temperature may have an impact on the mechanism of photocorrosion in alkaline environment. Comparing these results with those of the chemical stability of the material, the applied potential and light have a more dominant effect than temperature in the dissolution of species into the water (Fig. Figure S19 (d)-(e)-(f)). The accumulation of photogenerated holes at the surface of the photoanode in contact with the hydrated anion-exchange ionomer has a critical role in accelerating the photocorrosion reactions. The interpretation of the results is complicated because Bi, V and Mo are also in the stainless steel (SS) felt used as a substrate (Fig. Figure S12). The chemical dissolution of species in anion-exchange MPEAs is lower than of an SS felt coated with Mo:$BiVO_4$ and CoPi (without ionomer) left in a 0.01 M NaOH aqueous solution with pH ≈ 12 and even of the bare SS felt after annealing (Fig. Figure S20 (b)). However, a dominance of V dissolution with respect to Bi and Mo could be observed in all three cases. During OER in an alkaline environment, CoPi may experience a surface reconstruction which may affect its composition (towards the formation of Co oxides and hydroxides) and crystallinity.[80,81] This reconstruction may explain the immediate dissolution of cobalt into the hydrated anion-exchange ionomer and its transfer to the anodic reservoir right after the two initial characteristic curves both at 30 and 56 °C (Fig. 9). Temperature appears not to have any relevant effect on this process in contrast to the application of an external potential and light, as shown by the assessment of the chemical stability of CoPi (Fig. Figure S21).

View Article Online
DOI: 10.1039/D6SE00417B

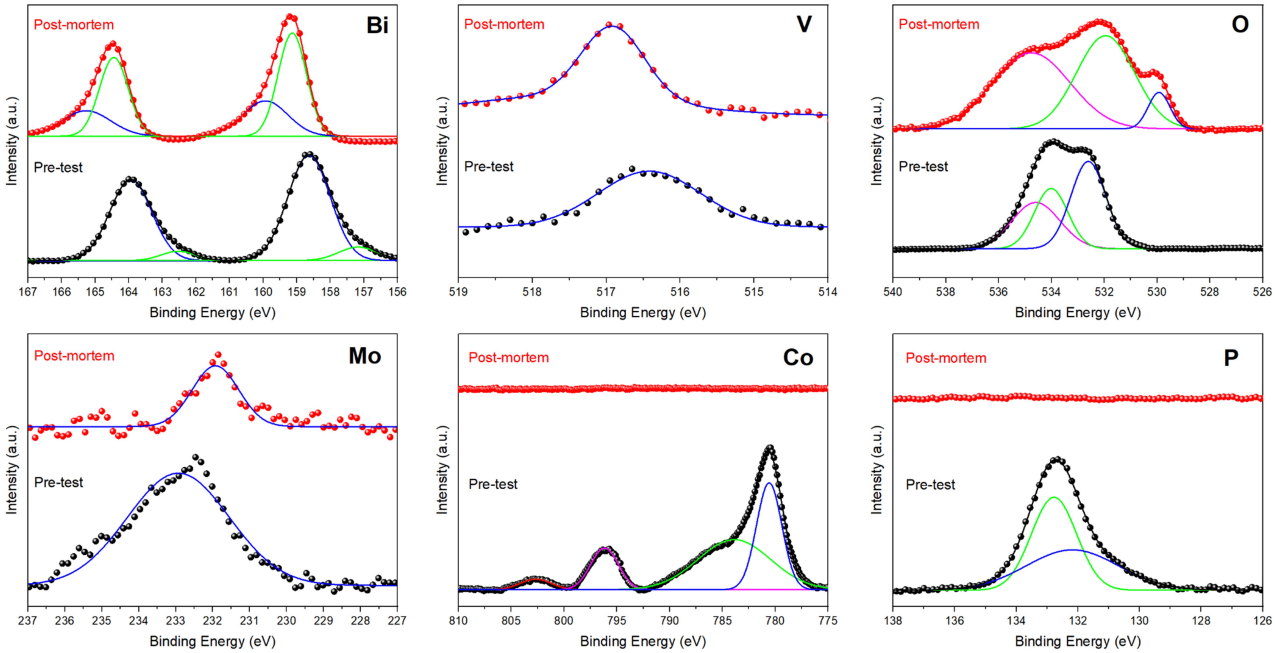

Fig. 7 XPS spectra of the pristine Mo:$BiVO_4$ with CoPi on titanium felt (black dots, as in Fig. 3) and of the Mo:$BiVO_4$ with CoPi covered by proton-exchange ionomer after the PEC tests in proton-exchange MPEA using liquid water at 30 °C for 15 hours (red dots) with the corresponding Lorentzian deconvolution for data fitting (lines) in the binding energy ranges for Bi, V, O, Mo, Co and P.

Fig. 10 compares the XPS spectra of pristine Mo:$BiVO_4$ samples with CoPi on SS felt with the same ones covered by anion-exchange ionomer after the PEC tests with liquid water at 30 °C in MPEA configuration. No relevant variations of the oxidation states of the different elements were observed, despite the complications in the analysis of the results caused by the elements which are in the SS felt (Fig. Figure S12). However, the primary effect of PEC tests can be attributed to the almost complete loss of Co 2p signals due to the co-catalyst dissolution.

The false-colour SEM images of the cross section of the anion-exchange membrane used for the tests at 30 °C show the formation of agglomerates in the order of 30 nm homogeneously distributed along its thickness (Fig. Figure S22). These agglomerates were only composed of C and Br, the main constituents of the Fumasep™ membrane, and therefore could not be associated to the photoanode dissolved species (Fig. Figure S23).

3.6 PEC characterizations with water vapour

Due to the inferior performance in liquid-phase water experiments of anion-exchange MPEAs compared to proton-exchange MPEAs, gas-phase tests were exclusively conducted with the latter ones. Operation with water in gas phase resulted in a comparable onset potentials to the ones obtained using liquid-phase water but a lower current density (approximately 85% lower at 1 V *vs.* RHE) (Fig. 11 (a)-(b)). This behaviour is attributed to the fact that gas-phase operation results in a worse hydration of the proton-exchange ionomer, reducing conductivity, and the reduced availability of water at the photoanode-electrolyte interface. The reduced membrane hydration also leads to a more acidic pH inside the nanochannels of the ionomer, potentially impacting the electrochemical reaction. The performance of pristine proton-exchange MPEAs with water vapour was unaffected by the flow field geometry or the imposed volumetric flow rate, which was varied from 20 to 220 mL min^{-1}. This suggests that water transport from the channels of the photo-electrolyzer to the active sites was not the limiting factor at these values of current density. Consequently, the geometry that minimizes the pressure gradient across the cell should be favoured. The photocorrosion of the material may be the cause of a faster reduction of the current density in time with respect to the one observed with liquid water (Fig. Figure S24). The lower local pH may induce more detrimental operating conditions, leading to faster photocorrosion and dissolution of the material.

4 Conclusions

The performance and the stability of membrane-photoelectrode assemblies with Mo-doped $BiVO_4$ photoanodes on metallic felts with CoPi co-catalyst were assessed for the first time using water in liquid and gas phase at different temperatures.

The optimal proton-exchange MPEAs tested with liquid water at different temperatures showed an increase in the onset potential with temperature from 0.77 V *vs.* RHE at 30 °C to 0.83 V *vs.* RHE at 56 °C, possibly due to a more pronounced surface recombination rate of photogenerated holes compared to their transfer to the electrolyte. The increase in saturation current density with temperature from 0.30 mA cm^{-2} at 30 °C to 0.40 mA cm^{-2} at 56 °C was explained by a decreased bandgap and increased absorption coefficients resulting in more light absorption and by the better reaction kinetics. The reduction of the saturation current density over time is attributed to the photocorrosion of the pho-

View Article Online
DOI: 10.1039/D6SE00417B

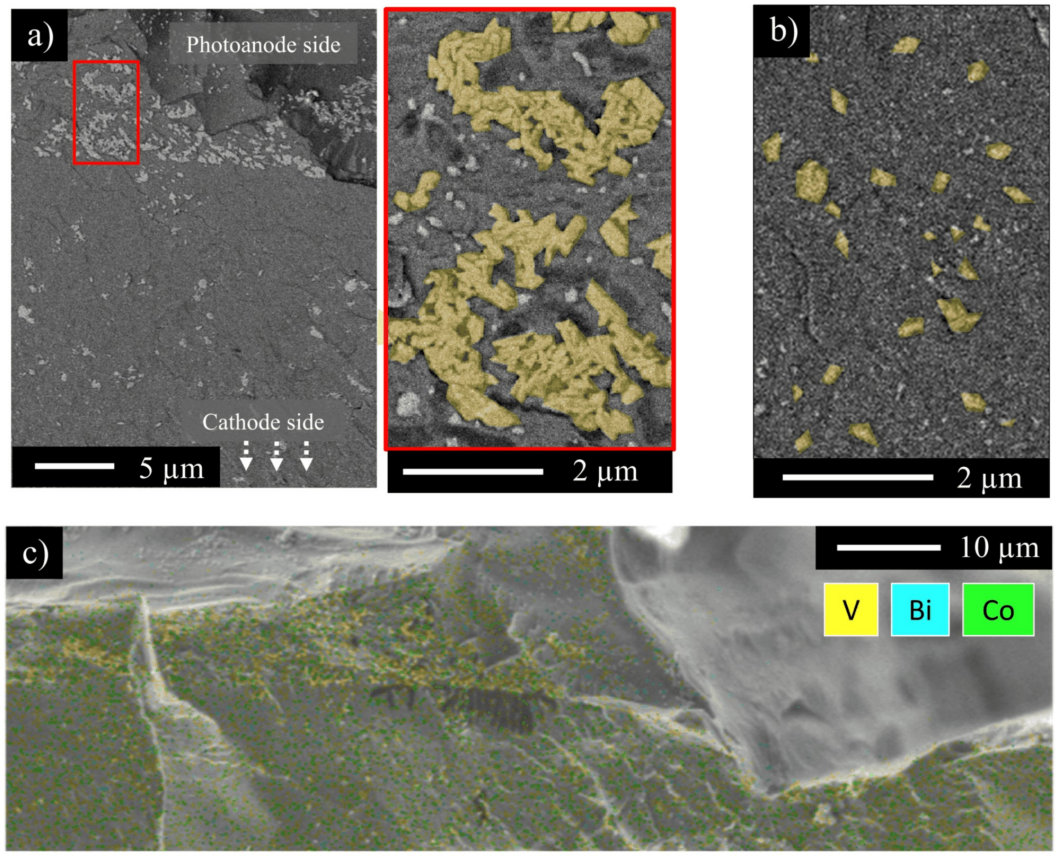

Fig. 8 (a)-(b) False-colour backscattered electron SEM images of the cross-section of the proton-exchange membrane after the tests with liquid water at 56 °C: (a) close to the photoanode on Ti felt (cathode not reported) with a zoom of a detail in a red rectangle; (b) at the middle of the membrane thickness. (c) EDXS elemental mapping of the cross-section SEM image showing the solid particles formed in the proton-exchange membrane after the PEC tests with liquid water at 56 °C.

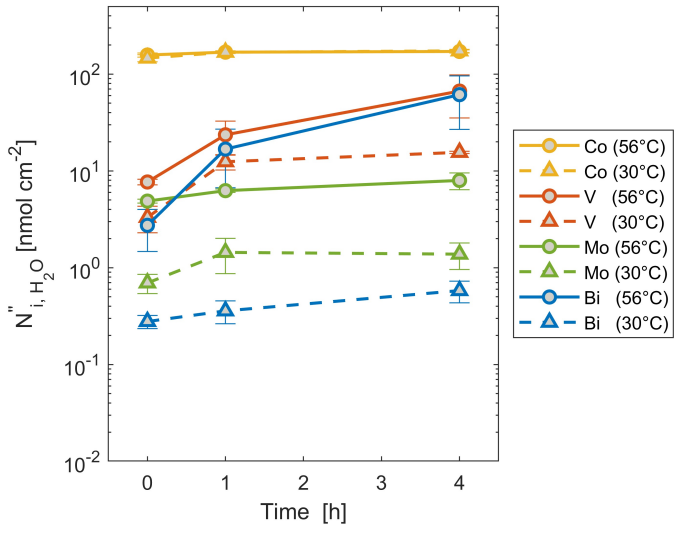

Fig. 9 Moles of Bi, V, Mo or Co dissolved in liquid water per illuminated geometric area of the felts after the chronoamperometry performed at different temperatures with anion-exchange MPEAs. The liquid samples were extracted after two potential-current density characteristic curves with simulated solar light.

toanode, which reduced the amount of photoactive material over time, thereby reducing the amount of absorbed light. The photocorrosion of the photoanode led to its dissolution, but it was more pronounced for V than Bi. The dissolved vanadium also formed solid particles in the proton-exchange membrane with diameters in the order of hundreds of nm, which coalesced in larger agglomerates of few μm in the region closer to the anodic side. The CoPi co-catalyst chemically dissolved due to the local acidic pH imposed by the proton-exchange ionomer.

With anion-exchange MPEAs, the saturation photocurrent density only reached 0.1 mA cm^{-2} at 30 °C. It decreased to 0.05 mA cm^{-2} at 56 °C. These reductions may be attributed to a less efficient charge extraction at the photoanode-electrolyte junction than with proton-exchange ionomer. The photocorrosion reactions caused the dissolution of Bi, V and Mo. The CoPi co-catalyst was completely dissolved after the first two potential-current density characteristic curves.

The performance of proton-exchange MPEAs with vapour was characterized by lower current densities with a reduction of 85% at 1 V *vs.* RHE and 30 °C, likely due to the worse hydration of the solid ionomer. Operation with vapour resulted in a faster decrease in the saturation current density during PEC tests than with liquid-phase water. The more acidic pH at the interface with the solid electrolyte possibly led to a faster photocorrosion and disso-

View Article Online
DOI: 10.1039/D6SE00417B

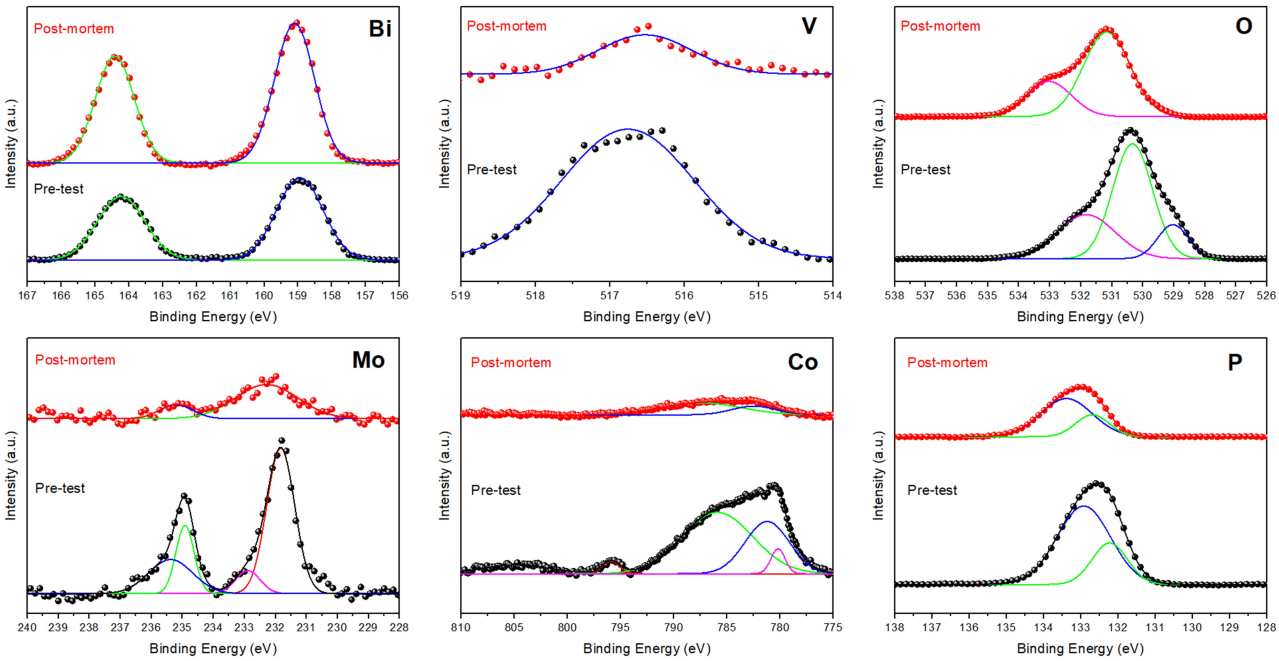

Fig. 10 XPS spectra of the pristine Mo:$BiVO_4$ with CoPi on stainless steel felt (black dots) and of the Mo:$BiVO_4$ with CoPi covered by anion-exchange ionomer after the PEC tests in anion-exchange MPEA using liquid water at 30 °C (red dots) with the corresponding Lorentzian deconvolution for data fitting (lines) in the binding energy ranges for Bi, V, O, Mo, Co and P.

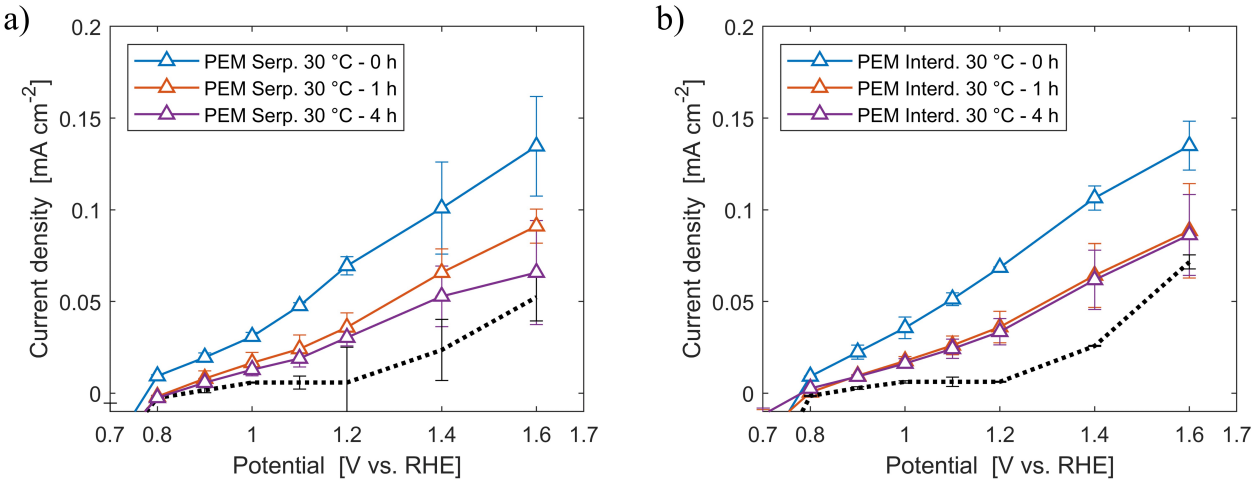

Fig. 11 (a)-(b) Current density-potential characteristic curves of pristine proton-exchange MPEAs and after different time spans of chronoamperometry at 1.23 V *vs.* RHE with water in gas phase at 30 °C using: (a) serpentine flow field geometry or (b) interdigitated flow field geometry. The black dotted lines in the figure represent the characteristic curves with water in gas phase of the pristine MPEAs in dark.

View Article Online
DOI: 10.1039/D6SE00417B

lution of the photoanode.

The deposition of solid ionomers onto the semiconductor enables operation of membrane-photoelectrode assemblies with liquid water and humid air at the expense of performance losses. Photocorrosion penalizes the operation of these devices and additional research work is required to identify the right combination of semiconductors and co-catalysts in order to reach the ambitious targets of durability required for the large-scale implementation of photoelectrochemical water splitting.

5 Authors contributions

R.V.: Conceptualization, Methodology, Investigation, Formal Analysis, Data Curation, Writing – original draft; S.G.: Conceptualization, Methodology, Investigation, Formal Analysis, Data Curation, Writing - review & editing; I.H.-G.and F.S.: Conceptualization, Methodology, Writing – review & editing; E.C.C.: Funding acquisition, Supervision, Writing – review & editing and S.H.: Funding acquisition, Conceptualization, Supervision, Project administration, Writing – review & editing.

6 Conflicts of interest

There are no conflicts of interest to declare.

7 Acknowledgements

This project was financially supported by the Swiss National Science Foundation with a Starting Grant (SCOUTS project, grant No. 155876) and a Sinergia grant #CRSII5_202225 (project DegPEC). It also received funding from the European Union's Horizon 2020 research and innovation program under the Marie-Skłodowska-Curie grant Solar2Chem (No. 861151) and the project Sun-to-X (No. 883264). The authors would like to thank: Gabriele Furlan of EPFL for the support in the development of the experimental setups; Laurent Chevalley from ATME mechanical workshop of EPFL for fruitful technical inputs during photoelectrolyzer cell design; Grégoire Baroz, Jérémie Bettex and Rita Therisod of the Interdisciplinary Center for Electron Microscopy (CIME) of EPFL for obtaining some SEM and TEM images of the samples; Riho Seljamäe-Green of the Advanced Characterization Team at Johnson Matthey Technology Centre and Mounir Driss Mensi of the X-Ray Diffraction and Surface Analytics Platform of EPFL for obtaining the XPS spectra; Sylvain Coudret of the Central Environmental Laboratory (GR-CEL) of EPFL for performing the ICP-MS measurements.

References

1 I. Holmes-Gentle, F. Alhersh, F. Bedoya-Lora and K. Hellgardt, *Photoelectrochemical Solar Cells*, John Wiley & Sons, Ltd, 2018, pp. 1–41.
2 I. Holmes-Gentle, F. Bedoya-Lora, F. Alhersh and K. Hellgardt, *The Journal of Physical Chemistry C*, 2019, **123**, 17–28.
3 S. Slade, S. A. Campbell, T. R. Ralph and F. C. Walsh, *Journal of The Electrochemical Society*, 2002, **149**, A1556.
4 M. Schalenbach, T. Hoefner, P. Paciok, M. Carmo, W. Lueke and D. Stolten, *The Journal of Physical Chemistry C*, 2015, **119**, 25145–25155.
5 F. Barbir, *Solar Energy*, 2005, **78**, 661–669.
6 I. R. E. Agency, *Green hydrogen cost reduction*, 2020.
7 M. Carmo, D. L. Fritz, J. Mergel and D. Stolten, *International Journal of Hydrogen Energy*, 2013, **38**, 4901–4934.
8 N. Du, C. Roy, R. Peach, M. Turnbull, S. Thiele and C. Bock, *Chemical Reviews*, 2022, **122**, 11830–11895.
9 S. A. Berlinger, B. D. McCloskey and A. Z. Weber, *The Journal of Physical Chemistry B*, 2018, **122**, 7790–7796.
10 F.-Y. Chen, Z.-Y. Wu, Z. Adler and H. Wang, *Joule*, 2021, **5**, 1704–1731.
11 European Chemical Agency (ECHA), *ECHA PFAS restriction proposal*, 2023, `https://echa.europa.eu/-/echa-publishes-pfas-restriction-proposal`.
12 J. Lim, J. M. Klein, S. G. Lee, E. J. Park, S. Y. Kang, S. Maurya, W. E. Mustain, S. Boettcher and Y. S. Kim, *ACS Energy Letters*, 2024, **9**, 3074–3083.
13 W. You, K. J. T. Noonan and G. W. Coates, *Progress in Polymer Science*, 2020, **100**, 101177.
14 P. Dias, A. Vilanova, T. Lopes, L. Andrade and A. Mendes, *Nano Energy*, 2016, **23**, 70–79.
15 M. Pourbaix, *Atlas of Electrochemical Equilibria in Aqueous Solutions*, National Association of Corrosion Engineers, 1974.
16 T. Stoll, G. Zafeiropoulos and M. N. Tsampas, *International Journal of Hydrogen Energy*, 2016, **41**, 17807–17817.
17 G. Zafeiropoulos, H. Johnson, S. Kinge, M. C. M. van de Sanden and M. N. Tsampas, *ACS Applied Materials & Interfaces*, 2019, **11**, 41267–41280.
18 M. V. Makarova, F. Amano, S. Nomura, C. Tateishi, T. Fukuma, Y. Takahashi and Y. E. Korchev, *ACS Catalysis*, 2022, **12**, 1201–1208.
19 G. Zafeiropoulos, P. Varadhan, H. Johnson, L. Kamphuis, A. Pandiyan, S. Kinge, M. C. M. van de Sanden and M. N. Tsampas, *ACS Applied Energy Materials*, 2021, **4**, 9600–9610.
20 C. X. M. Ta, C. Akamoto, Y. Furusho and F. Amano, *ACS Sustainable Chemistry & Engineering*, 2020, **8**, 9456–9463.
21 M. Caretti, E. Mensi, R.-A. Kessler, L. Lazouni, B. Goldman, L. Carbone, S. Nussbaum, R. A. Wells, H. Johnson, E. Rideau, J.-h. Yum and K. Sivula, *Advanced Materials*, 2023, **35**, 2208740.
22 M. S. Prévot and K. Sivula, *The Journal of Physical Chemistry C*, 2013, **117**, 17879–17893.
23 A. S. Aricò, M. Girolamo, S. Siracusano, D. Sebastian,

View Article Online
DOI: 10.1039/D6SE00417B

V. Baglio and M. Schuster, *Membranes*, 2017, **7**, 25.

24 D. O. B. Apriandanu, R. M. Surya, K. Beppu and F. Amano, *ACS Applied Energy Materials*, 2023, **6**, 10736–10741.

25 F. Amano, R. M. Surya and S. P. Singh, *ChemElectroChem*, 2024, **11**, e202300646.

26 M. Ben-Naim, R. J. Britto, C. W. Aldridge, R. Mow, M. A. Steiner, A. C. Nielander, L. A. King, D. J. Friedman, T. G. Deutsch, J. L. Young and T. F. Jaramillo, *ACS Energy Letters*, 2020, **5**, 2631–2640.

27 H. Kim, J. W. Seo, W. Chung, G. M. Narejo, S. W. Koo, J. S. Han, J. Yang, J.-Y. Kim and S.-I. In, *ChemSusChem*, 2023, **16**, e202202017.

28 R. Lin, Y. Lu, J. Xu, J. Huo and X. Cai, *Applied Energy*, 2022, **326**, 120011.

29 S. Toghyani, E. Afshari, E. Baniasadi and S. A. Atyabi, *Electrochimica Acta*, 2018, **267**, 234–245.

30 D. Lee, M. Kim, J. Kim, I. Moon and J. Kim, *International Journal of Hydrogen Energy*, 2024, **88**, 322–332.

31 F. M. Toma, J. K. Cooper, V. Kunzelmann, M. T. McDowell, J. Yu, D. M. Larson, N. J. Borys, C. Abelyan, J. W. Beeman, K. M. Yu, J. Yang, L. Chen, M. R. Shaner, J. Spurgeon, F. A. Houle, K. A. Persson and I. D. Sharp, *Nature Communications*, 2016, **7**, 12012.

32 D. K. Lee and K.-S. Choi, *Nature Energy*, 2018, **3**, 53–60.

33 S. Zhang, M. Rohloff, O. Kasian, A. M. Mingers, K. J. J. Mayrhofer, A. Fischer, C. Scheu and S. Cherevko, *The Journal of Physical Chemistry C*, 2019, **123**, 23410–23418.

34 S. Zhang, I. Ahmet, S.-H. Kim, O. Kasian, A. M. Mingers, P. Schnell, M. Kölbach, J. Lim, A. Fischer, K. J. J. Mayrhofer, S. Cherevko, B. Gault, R. van de Krol and C. Scheu, *ACS Applied Energy Materials*, 2020, **3**, 9523–9527.

35 C. X. M. Ta, Y. Furusho and F. Amano, *Applied Surface Science*, 2021, **548**, 149251.

36 I. Holmes-Gentle, F. E. Bedoya-Lora, L. Aimone and S. Haussener, *Journal of Materials Chemistry A*, 2023, **11**, 23895–23908.

37 C. Zachäus, F. F. Abdi, L. M. Peter and R. v. d. Krol, *Chemical Science*, 2017, **8**, 3712–3719.

38 J.-W. Jang, D. Friedrich, S. Müller, M. Lamers, H. Hempel, S. Lardhi, Z. Cao, M. Harb, L. Cavallo, R. Heller, R. Eichberger, R. van de Krol and F. F. Abdi, *Advanced Energy Materials*, 2017, **7**, 1701536.

39 I. Y. Ahmet, Y. Ma, J.-W. Jang, T. Henschel, B. Stannowski, T. Lopes, A. Vilanova, A. Mendes, F. F. Abdi and R. v. d. Krol, *Sustainable Energy & Fuels*, 2019, **3**, 2366–2379.

40 R. Valenza, I. Holmes-Gentle, F. E. Bedoya-Lora and S. Haussener, *Sustainable Energy & Fuels*, 2024.

41 H. Dotan, K. Sivula, M. Grätzel, A. Rothschild and S. C. Warren, *Energy & Environmental Science*, 2011, **4**, 958–964.

42 G. Hinds and E. Brightman, *Electrochemistry Communications*, 2012, **17**, 26–29.

43 M. Cecchetti, A. Casalegno and M. Zago, *Journal of Power Sources*, 2018, **400**, 218–224.

44 Q. Xu, S. Z. Oener, G. Lindquist, H. Jiang, C. Li and S. W. Boettcher, *ACS Energy Letters*, 2021, **6**, 305–312.

45 C. Rabissi, E. Brightman, G. Hinds and A. Casalegno, *International Journal of Hydrogen Energy*, 2018, **43**, 9797–9802.

46 H. R. Zamanizadeh, S. Sunde, B. G. Pollet and F. Seland, *Electrochimica Acta*, 2022, **424**, 140561.

47 J. K. Cooper, S. Gul, F. M. Toma, L. Chen, Y.-S. Liu, J. Guo, J. W. Ager, J. Yano and I. D. Sharp, *The Journal of Physical Chemistry C*, 2015, **119**, 2969–2974.

48 P. Makuła, M. Pacia and W. Macyk, *The Journal of Physical Chemistry Letters*, 2018, **9**, 6814–6817.

49 A. Yengantiwar, S. Palanivel, P. S. Archana, Y. Ma, S. Pan and A. Gupta, *The Journal of Physical Chemistry C*, 2017, **121**, 5914–5924.

50 F. F. Abdi, N. Firet and R. van de Krol, *ChemCatChem*, 2013, **5**, 490–496.

51 T. Lopes, L. Andrade, F. L. Formal, M. Gratzel, K. Sivula and A. Mendes, *Physical Chemistry Chemical Physics*, 2014, **16**, 16515–16523.

52 F. F. Abdi, T. J. Savenije, M. M. May, B. Dam and R. v. d. Krol, *The Origin of Slow Carrier Transport in BiVO4 Thin Film Photoanodes: A Time-Resolved Microwave Conductivity Study*, 2013, `https://pubs.acs.org/doi/full/10.1021/jz4013257`, Archive Location: world.

53 A. J. E. Rettie, H. C. Lee, L. G. Marshall, J.-F. Lin, C. Capan, J. Lindemuth, J. S. McCloy, J. Zhou, A. J. Bard and C. B. Mullins, *Combined Charge Carrier Transport and Photoelectrochemical Characterization of BiVO4 Single Crystals: Intrinsic Behavior of a Complex Metal Oxide*, 2013, `https://pubs.acs.org/doi/full/10.1021/ja405550k`, Archive Location: world.

54 S. K. Pilli, T. E. Furtak, L. D. Brown, T. G. Deutsch, J. A. Turner and A. M. Herring, *Energy & Environmental Science*, 2011, **4**, 5028–5034.

55 Y. Zhang, D. Wang, X. Zhang, Y. Chen, L. Kong, P. Chen, Y. Wang, C. Wang, L. Wang and Y. Liu, *Electrochimica Acta*, 2016, **195**, 51–58.

56 F. J. Knorr, C. C. Mercado and J. L. McHale, *The Journal of Physical Chemistry C*, 2008, **112**, 12786–12794.

57 Y. Shi, Z.-R. Ma, Y.-Y. Xiao, Y.-C. Yin, W.-M. Huang, Z.-C. Huang, Y.-Z. Zheng, F.-Y. Mu, R. Huang, G.-Y. Shi, Y.-Y. Sun, X.-H. Xia and W. Chen, *Nature Communications*, 2021, **12**, 3021.

58 S. Wang, T. He, P. Chen, A. Du, K. K. Ostrikov, W. Huang and L. Wang, *Advanced Materials*, 2020, **32**, 2001385.

59 K. Zhang, B. Jin, C. Park, Y. Cho, X. Song, X. Shi, S. Zhang, W. Kim, H. Zeng and J. H. Park, *Nature Communications*, 2019, **10**, 2001.

60 S. Saha, D. Maity, D. Pal, D. Sarkar, D. De, G. G. Khan and K. Mandal, *ACS Applied Nano Materials*, 2023, **6**, 21385–21394.

61 L. Pan, J. Wu, X. Xu, F. Lv, Y. Chen and L. Guo, *International Journal of Hydrogen Energy*, 2023, **48**, 13479–13488.

62 E. M. P. Steinmiller and K.-S. Choi, *Proceedings of the National Academy of Sciences*, 2009, **106**, 20633–20636.

View Article Online
DOI: 10.1039/D6SE00417B

63 R. Zhao, Y. Zhou, P. Guo, R. Mo, Y. Tang and H. Li, *Advanced Science*, 2025, **12**, e09037.
64 B. Liu, X. Wang, Y. Zhang, M. Zhu, C. Zhang, S. Li, Y. Ma, W. Huang and S. Wang, *Nature Communications*, 2025, **16**, 2792.
65 C. Zhou, L. Zhang, X. Tong and M. Liu, *ACS Applied Materials & Interfaces*, 2021, **13**, 61227–61236.
66 Y. P. Varshni, *Physica*, 1967, **34**, 149–154.
67 C. Hill, M. C. Weber, J. Lehmann, T. Leinen, M. Fiebig, J. Kreisel and M. Guennou, *APL Materials*, 2020, **8**, 081108.
68 D.-H. Ha, B. Han, M. Risch, L. Giordano, K. P. C. Yao, P. Karayaylali and Y. Shao-Horn, *Nano Energy*, 2016, **29**, 37–45.
69 S. Gupta, R. Singh, M. D. Anoop, V. Kulshrestha, D. N. Srivastava, K. Ray, S. L. Kothari, K. Awasthi and M. Kumar, *Applied Physics A*, 2018, **124**, 737.
70 F. Xie, W. C. H. Choy, C. Wang, X. Li, S. Zhang and J. Hou, *Advanced Materials*, 2013, **25**, 2051–2055.
71 I. Povar, O. Spinu, I. Zinicovscaia, B. Pintilie and S. Ubaldini, *Journal of Electrochemical Science and Engineering*, 2019, **9**, 75–84.
72 K. Post and R. G. Robins, *Electrochimica Acta*, 1976, **21**, 401–405.
73 *CRC Handbook of Chemistry and Physics*, ed. W. M. Haynes, CRC Press, Boca Raton, 97th edn, 2016.
74 S. Kundu, M. Cimenti, S. Lee and D. Bessarabov, *Membrane Technology*, 2009, **2009**, 7–10.
75 K. Yasuda, A. Taniguchi, T. Akita, T. Ioroi and Z. Siroma, *Physical Chemistry Chemical Physics*, 2006, **8**, 746–752.
76 W. Bi, G. E. Gray and T. F. Fuller, *Electrochemical and Solid-State Letters*, 2007, **10**, B101.
77 T. Jahnke, G. A. Futter, A. Baricci, C. Rabissi and A. Casalegno, *Journal of The Electrochemical Society*, 2019, **167**, 013523.
78 H. Yu, L. Bonville, J. Jankovic and R. Maric, *Applied Catalysis B: Environmental*, 2020, **260**, 118194.
79 Z. Zeng, R. Ouimet, L. Bonville, A. Niedzwiecki, C. Capuano, K. Ayers, A. P. Soleymani, J. Jankovic, H. Yu, G. Mirshekari, R. Maric and S. Bliznakov, *Journal of The Electrochemical Society*, 2022, **169**, 054536.
80 Y. Zhan, S. Yang, M. Lu, Z. Liu and J. Y. Lee, *Electrochimica Acta*, 2017, **227**, 310–316.
81 X. Zhang, Q. Hou, S. Cao, X. Lin, X. Chen, Z. Wang, S. Wei, S. Liu, F. Dai and X. Lu, *Green Chemistry*, 2023, **25**, 7883–7903.

View Article Online
DOI: 10.1039/D6SE00417B

Data availability statement

The data supporting this article will been included as part of the Supplementary Information.